INTERNATIONAL JOURNAL OF ROBUST AND NONLINEAR CONTROL
Int. J. Robust Nonlinear Control 2009; **19**:512–531
Published online 23 April 2008 in Wiley InterScience (www.interscience.wiley.com). DOI: 10.1002/rnc.1328

A hybrid controller design for bi-axial inverted pendulum system

Long-Hong Chang[1] and An-Chen Lee[2,*,†]

[1]*Department of Automation Engineering, Ta Hwa Institute of Technology, No. 1, Dahua Road, Qionglin Shiang Hsinchu County 307-40, Taiwan, Republic of China*
[2]*Department of Mechanical Engineering, National Chiao Tung University, 1001 Ta Hsueh Road, Hsinchu 300-10, Taiwan, Republic of China*

SUMMARY

This study presents the use of Tustin's friction model and a disturbance observer (DOB) to improve the steady-state error (SSE) of a bi-axial inverted pendulum–cart system (IPCS). Furthermore, a hybrid controller contains a feedback linearization control for pendulum angle in the region of 3–12° to enlarge the angle of operation and an H_∞ control using loop shaping design procedure (LSDP) for cart position and pendulum angle in the region of 0–3° to stabilize the IPCS, respectively. Experimental results reveal that the pendulum maximum angle of operation is improved from 7 to 12°; the SSE of the angle of the pendulum is reduced from 0.85 to 0.1°, and the SSE of the position of the cart is reduced from 10 to 1.4 mm. Experimental results are illustrated and films are provided at the web site http://hinfinity.myweb.hinet.net to show the effectiveness and robustness of the hybrid controller with Tustin's friction model and DOB compensation. Copyright © 2008 John Wiley & Sons, Ltd.

Received 22 July 2007; Revised 12 March 2008; Accepted 16 March 2008

KEY WORDS: inverted pendulum; friction compensation; disturbance observer; loop shaping design procedure; H_∞

1. INTRODUCTION

Many approaches have been applied to inverted pendulum–cart systems (IPCSs). Furuta *et al.* [1] used linear state feedback with an integrator controller to regulate a double-inverted pendulum on an inclined rail. Tsachouridis and Medrano-Cerda [2] implemented an H_∞ controller via a robust reduced-order dynamic observer with an integrator to control a triple-inverted pendulum on an inclined rail. Chen *et al.* [3] used sliding-mode control (SMC) to erect a parallel-rod IPCS. Some papers [4–8] performed different two-phase hybrid control to swing-up and stabilize an IPCS from the pendant position. A hammer was adopted in [7] to cause an external disturbance force to

*Correspondence to: An-Chen Lee, Department of Mechanical Engineering, National Chiao Tung University, 1001 Ta Hsueh Road, Hsinchu 300-10, Taiwan, Republic of China.
†E-mail: aclee@mail.nctu.edu.tw

demonstrate the robustness of the system. Sprenger *et al.* [9] balanced a 2D IPCS on a two-joint rotational robot. They further compared the performance of three pendulum angle sensors and concluded that the encoder is the best followed by the Hall effect sensor with the potentiometer least favored. Cho and Jung [10] presented decentralized neural network for a circular trajectory position tracking control while balancing a 2D IPCS on an X–Y table. Similar to [10], Wai and Chang [11] used decentralized adaptive SMC to track a periodic sinusoidal command. However, no clear experimental data were shown. The decentralized control of [9–11] treats the coupling effects of a 2D IPCS as a disturbance. van der Linden and Lambrechts [12] implemented an H_∞ controller to eliminate the dry frictional force between the cart and the rail to stabilize an IPCS. Grasser *et al.* [13] built a revolutionary two-wheeled IPCS that can perform stationary U-turns. Many experimental films are provided at their web site to show the performances of the revolution machine. Table I shows the control strategies, types of pendulum and friction compensation methods used in the reference papers described above. As for the newly developed control algorithms, Olfati-Saber [14] developed a fixed point backstepping procedure for global/semiglobal stabilization of an IPCS. Aguilar-Ibañez and Gutierrez [15] presented a simple model matching controller for stabilization

Table I. Control strategies in the references and this study.

Reference	Control strategy	Pendulum dimension/rod	Friction compensation	Photo/film
1	Linear state feedback with integrator	1D/2 rods, inclined rail	Viscous model	Photo
2	H_∞ control with integrator	1D/3 rods, inclined rail	No	No
3	Sliding-mode control	1D/2 rods, parallel rods	No	No
4	Fuzzy (swing-up) and linear state feedback	1D/1 rod	No	Photo
5	Fuzzy (swing-up) and adaptive sliding mode	1D/1 rod	Coulomb/bounded uncertainty	No
6	Energy approach (swing-up) and linear state feedback	1D/1 rod	No	No
7	Gray prediction (swing-up) and PD (hammer impact)	1D/1 rod	Coulomb/bounded uncertainty	Photo
8	Quasi-zero torque trajectory (swing-up) and linear quadratic regulator	1D/2 rods	No	Photo/film
9	Linear state feedback (decentralized algorithm)	2D/1 rod	Coulomb+viscous model	Photo
10	Neural networks (decentralized algorithm)	2D/1 rod	No	Photo
11	Adaptive sliding-mode (decentralized algorithm)	2D/1 rod	No	No
12	H_∞ control	1D/1 rod	Coulomb/bounded uncertainty	No
13	Pole-assignment	1D/1 rod	No	Photo/film
This study	Hybrid control with performance specification list (9 V battery impact) (ball balancing)	2d/1 rod, inclined rail (shown in film)	Coulomb+stiction+ Stribeck+viscous model and DOB	Photo/film

DOI: 10.1002/rnc

the IPCS. In [16, 17] a Lyapunov function combined with LaSalle's invariance principle was proposed to stabilize a 1D/2D IPCS. The simulation results in [14–17] showed that the IPCSs have a very large attraction domain over the upper half-plane and a very slow time convergence.

However, most authors have focused on the control law, in either the swing-up or the stabilizing region. The frictional forces that may degrade the system performance are usually ignored or treated as a bounded uncertainty. Some works considered friction compensation, but only for Coulomb and/or viscous forces. The authors' observations show that Coulomb and/or viscous friction are not the only existing forces that can cause undesirable phenomena such as stick–slip oscillation, poor tracking performance and steady-state error (SSE).

In this study, Tustin's friction model [18–20] and a disturbance observer (DOB) [21] are proposed to compensate for the friction and disturbance between the cart and the rail to reduce the SSE of the IPCS. Then, a hybrid controller is employed, which contains the following:

1. A feedback linearization control for pendulum angle. The approach has the advantages on the maximum angle of operation and system robustness in the region of 3–12°.
2. An H_∞ control using loop shaping design procedure (LSDP) is performed to stabilize the cart position and pendulum angle of the IPCS in the region of 0–3°. The advantage is that LSDP dose not require γ-iteration for its solution, and explicit formulas for the corresponding controllers are available.

The overall control system shown in Figure 1 consists the following elements: the $\alpha\beta$-filter [22] used to estimate the cart velocity $\dot{\mathbf{x}}$ and the pendulum angular velocity $\dot{\Theta}$; Tustin's friction model and a DOB based on the cart velocity loop proposed to compensate for the frictional force $\mathbf{f}$ and disturbance $\mathbf{d}$ between the cart and the rail of the IPCS; the Mux block combining vector signals into larger vector; the Demux block splitting vector signal into smaller vectors; the hybrid control designed to eliminate the nonlinear and unstable characteristics of the system; the final control signals through the 16-bit digital-to-analog converter (DAC) and the motor driver with servo gain $\mathbf{K}_a\mathbf{K}_t\mathbf{K}_n$ applied to control the bi-axial IPCS. The experimental results show that the proposed approach effectively controls the system.

The experimental setup of the bi-axial IPCS includes the following.

1. A cart moving within an operation range 320×320 mm on a ball-screw-driven X–Y table, where the X-axis is on the top.
2. A pendulum with a maximum angle of inclination $\pm 18°$ hinged on a universal joint so as to rotate freely in the 2D working space. Two 1800-Pulse/Rev incremental optical encoders with an angular resolution of 0.05° are used to measure the angles of the pendulum.
3. Two 300 W DC motors with 1000-Pulse/Rev encoders used as actuators to drive the cart on the X–Y table through the ball screw. Since the pitch of the ball screw is 5 mm, the resolution of the cart's horizontal displacement is 1.25 μm.
4. In torque mode, two motor drivers applied to actuate the DC motors with the following specifications; maximum input voltage is ± 10 V and maximum output current is 15 A (transient) and 5 A (continuous).
5. A 4-axis motion control card connected between a PC and the IPCS to record the angles of the pendulum and the positions of the cart, and to send DAC signals to the motor drivers.
6. AMD K6-2 500 MHz PC as the host computer and the control algorithm written in Borland C++ 3.1 with a sampling rate of 500 Hz.

The remainder of the paper is organized as follows: Section 2 deals with modeling the bi-axial IPCS. In Section 3, Tustin's friction model and the DOB are addressed to compensate for the

DOI: 10.1002/rnc

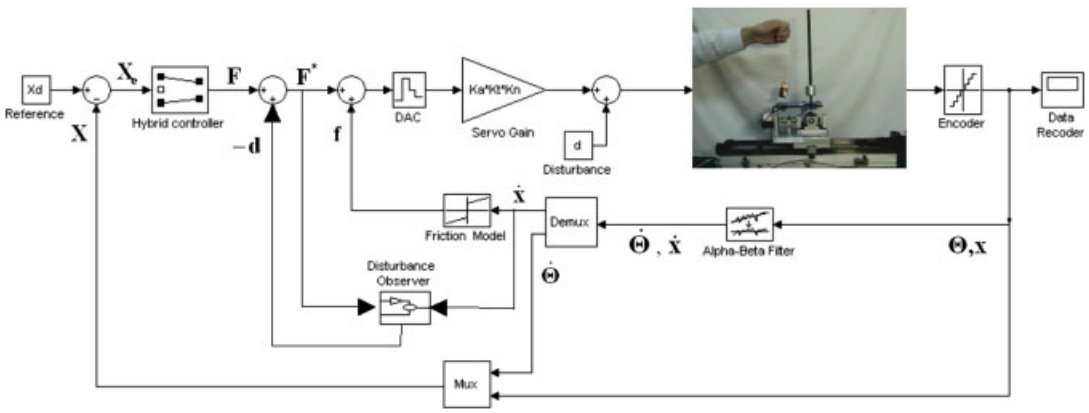

Figure 1. Whole control loop of the bi-axial inverted pendulum system.

friction and disturbance between the cart and rail. The hybrid controller is described in Section 4. In Section 5, the experiments show the effectiveness and robustness of the control schema. Section 6 discusses the system with friction and DOB compensation results. The final conclusion is drawn in Section 7.

2. SYSTEM MODELING

The 2D IPCS as shown in Figure 2 is adopted to formulate the equations of motion. Tables II and III are the nomenclature and values of the real system. The equations of motion are obtained by using the Euler–Lagrange formulation [1]:

$$\begin{bmatrix}\ddot{x}\\ \ddot{y}\end{bmatrix}=\begin{bmatrix}c_3c_0 & -c_3c_1\\ -\bar{c}_3\bar{c}_1 & \bar{c}_3\bar{c}_0\end{bmatrix}\begin{bmatrix}(F_x-f_x)\\ (F_y-f_y)\end{bmatrix}+\begin{bmatrix}c_3c_2\\ \bar{c}_3\bar{c}_2\end{bmatrix} \tag{1a}$$

$$\begin{bmatrix}\ddot{\theta}\\ \ddot{\phi}\end{bmatrix}=\begin{bmatrix}-c_4c_6c_3c_0 & c_4c_6c_3c_1\\ \bar{c}_4\bar{c}_6\bar{c}_3\bar{c}_1 & -\bar{c}_4\bar{c}_6\bar{c}_3\bar{c}_0\end{bmatrix}\begin{bmatrix}(F_x-f_x)\\ (F_y-f_y)\end{bmatrix}+\begin{bmatrix}-c_4c_6c_3c_2+c_4c_5-c_4\tau_\theta\\ -\bar{c}_4\bar{c}_6\bar{c}_3\bar{c}_2+\bar{c}_4\bar{c}_5-\bar{c}_4\tau_\phi\end{bmatrix} \tag{1b}$$

where $k_{0x}=m_{0x}+m_1+m_2$, $k_{0y}=m_{0y}+m_1+m_2$, $k_1=m_1l_1+m_2l_2$, $k_2=J_1+J_2+m_1l_1^2+m_2l_2^2$,

$$\Delta_x=k_{0x}k_2-k_1^2\cos^2\theta,\quad \Delta_y=k_{0y}k_2-k_1^2\cos^2\phi,\quad c_0=k_2\Delta_y\cos\phi,\quad c_1=k_1^2k_2\cos^2\phi\sin\phi\sin\theta$$

$$\begin{aligned}c_2=&\,k_1\Delta_y\cos\theta\cdot\tau_\theta-k_{0y}k_1k_2\cos\phi\sin\phi\sin\theta\cdot\tau_\phi\\ &+k_1k_2\Delta_y\cos\phi[\cos\phi\sin\theta(\dot{\theta}^2+\dot{\phi}^2)+2\dot{\theta}\dot{\phi}\sin\phi\cos\theta]\\ &+k_{0y}k_1k_2\cos\phi\sin^2\phi\sin\theta(k_1g\cos\theta-k_2\dot{\theta}^2\cos\phi)-k_1^3k_2\cos^2\phi\sin^2\phi\sin\theta\dot{\phi}^2\\ &-k_1\Delta_y\cos\phi\cos\theta(k_1g\sin\theta+2k_2\dot{\phi}\dot{\theta}\sin\phi)\end{aligned}$$

$$c_3=(\Delta_x\Delta_y\cos\phi-k_{0y}k_1^2k_2\cos\phi\sin^2\phi\sin^2\theta)^{-1},\quad c_4=(k_2\cos\phi)^{-1}$$

$$c_5=k_1g\sin\theta+2k_2\dot{\phi}\dot{\theta}\sin\phi,\quad c_6=k_1\cos\theta$$

DOI: 10.1002/rnc

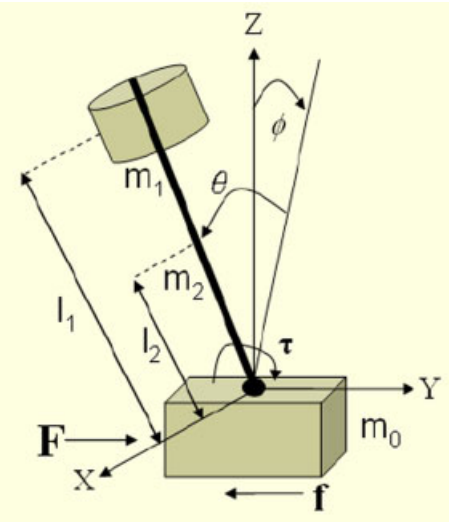

Figure 2. Coordination of the 2D inverted pendulum system.

and $\bar{c}_i$ can be obtained by interchanging (x, θ) with (y, ϕ) in c_i, i.e.

$$\bar{c}_0 = k_2 \Delta_x \cos\theta, \quad \bar{c}_1 = k_1^2 k_2 \cos^2\theta \sin\theta \sin\phi$$

$$\begin{aligned}\bar{c}_2 = {} & k_1 \Delta_x \cos\phi \cdot \tau_\phi - k_{0x} k_1 k_2 \cos\theta \sin\theta \sin\phi \cdot \tau_\theta \\ & + k_1 k_2 \Delta_x \cos\theta [\cos\theta \sin\phi (\dot{\phi}^2 + \dot{\theta}^2) + 2\dot{\phi}\dot{\theta} \sin\theta \cos\phi] \\ & + k_{0x} k_1 k_2 \cos\theta \sin^2\theta \sin\phi (k_1 g \cos\phi - k_2 \dot{\phi}^2 \cos\theta) \\ & - k_1^3 k_2 \cos^2\theta \sin^2\theta \sin\phi \dot{\theta}^2 \\ & - k_1 \Delta_x \cos\theta \cos\phi (k_1 g \sin\phi + 2 k_2 \dot{\theta}\dot{\phi} \sin\theta)\end{aligned}$$

$$\bar{c}_3 = (\Delta_y \Delta_x \cos\theta - k_{0x} k_1^2 k_2 \cos\theta \sin^2\theta \sin^2\phi)^{-1}, \quad \bar{c}_4 = (k_2 \cos\theta)^{-1}$$

$$\bar{c}_5 = k_1 g \sin\phi + 2 k_2 \dot{\theta}\dot{\phi} \sin\theta, \quad \bar{c}_6 = k_1 \cos\phi$$

In the text, the following symbols are defined:

$$\mathbf{x} = [x \;\; y]^{\mathrm{T}}, \quad \mathbf{\Theta} = [\theta \;\; \phi]^{\mathrm{T}}, \quad \mathbf{F} = [F_x \;\; F_y]^{\mathrm{T}}, \quad \mathbf{f} = [f_x \;\; f_y]^{\mathrm{T}}, \quad \boldsymbol{\tau} = [\tau_\theta \;\; \tau_\phi]^{\mathrm{T}}$$

$$\mathbf{K}_{\mathrm{a}} = [K_{\mathrm{a}x} \;\; K_{\mathrm{a}y}]^{\mathrm{T}}$$

$$\mathbf{X}_{\mathrm{d}} = \begin{bmatrix} \theta_{\mathrm{d}} & \dot{\theta}_{\mathrm{d}} & x_{\mathrm{d}} \\ \phi_{\mathrm{d}} & \dot{\phi}_{\mathrm{d}} & y_{\mathrm{d}} \end{bmatrix}^{\mathrm{T}}, \quad \mathbf{X} = \begin{bmatrix} \theta & \dot{\theta} & x \\ \phi & \dot{\phi} & y \end{bmatrix}^{\mathrm{T}}$$

From (1), it is observed that the frictional force $\mathbf{f}$ and the joint frictional torque $\boldsymbol{\tau}$ will degrade the performance of the IPCS.

DOI: 10.1002/rnc

Table II. Nomenclature.

Symbol	Description
x/y	Position of the cart at the X/Y-axis
θ/ϕ	Angle of pendulum about the X/Y direction
F_x/F_y	Control force on the X/Y-axis
f_x/f_y	Frictional force on the X/Y-axis
τ_θ/τ_ϕ	Joint frictional torque in the θ/ϕ direction
m_{0x}/m_{0y}	Cart mass of the X/Y-axis
m_1	Pendulum head mass
m_2	Rod mass
$m_{\mathrm{eq}}=m_1+m_2$	Equivalent mass of the pendulum
M	The summation of the cart mass and m_{eq}
l_1	Length of the pendulum from the head to the cart
l_2	Half-length of the rod
l_{eq}	Equivalent length of the pendulum
r_1	Radius of the pendulum head
r_2	Rod radius
r_{joint}	Bearing radius of the joint
J_1	Moment of inertia of the pendulum head with respect to the cart
J_2	Moment of inertia of the rod with respect to the cart
$K_{\mathrm{a}x}/K_{\mathrm{a}y}$	Amplifier gain of X/Y axis
K_{t}	Motor torque constant
K_{n}	Ball screw transfer factor
K_{p}	Gain
T_{c}	Coulomb force between the cart and the rail
T_{s}	Stiction force between the cart and the rail
T_{d}	Viscous damping coefficient between the cart and the rail
v_{s}	Stribeck velocity constant
v	Cart velocity
$j_{\mathrm{d}_x}/j_{\mathrm{d}_y}$	Joint viscous damping coefficient in the X/Y direction
$j_{\mathrm{c}_x}/j_{\mathrm{c}_y}$	Joint Coulomb force in the X/Y direction

3. TUSTIN'S FRICTION MODEL AND THE DOB

The static Tustin's friction model and the DOB are employed to compensate for the friction and disturbance between the cart and the rail. Considering the resolution of the cart's horizontal displacement is 1.25 μm, one employs Tustin's model to model the frictional force (neglecting the presliding effect) in cart–rail. Tustin's model shown in Figure 3 comprises Coulomb force T_{c}, stiction force T_{s}, Stribeck force $(T_{\mathrm{s}}-T_{\mathrm{c}})\mathrm{e}^{-(v/v_{\mathrm{s}})}$ and viscous force $T_{\mathrm{d}}v$, and it is expressed as follows:

$$f=T_{\mathrm{c}}+(T_{\mathrm{s}}-T_{\mathrm{c}})\mathrm{e}^{-(v/v_{\mathrm{s}})}+T_{\mathrm{d}}v \tag{2}$$

In Tustin's model, the schema shown in Figure 4 is used to establish the friction–velocity map. Since steady-state velocity is concerned to obtain the friction–velocity map, the effect of phase shift induced by DAC, encoder and $\alpha\beta$-filter is negligible in the case. The dynamic equation of the velocity feedback system for Figure 4 is

$$M\dot{v}+(T_{\mathrm{d}}+K_{\mathrm{p}}K_{\mathrm{a}}K_{\mathrm{t}}K_{\mathrm{n}})v+T_{\mathrm{f}}=K_{\mathrm{p}}K_{\mathrm{a}}K_{\mathrm{t}}K_{\mathrm{n}}u \tag{3}$$

where $T_{\mathrm{f}}=T_{\mathrm{c}}+(T_{\mathrm{s}}-T_{\mathrm{c}})\mathrm{e}^{-(v/v_{\mathrm{s}})}$.

DOI: 10.1002/rnc

Table III. Parameters of the real system.

m_{0x}	3.1 kg
m_{0y}	14.2 kg
m_1	0.25 kg
m_2	0.05 kg
m_{eq}	0.3 kg
l_1	0.32 m
l_2	0.1675 m
l_{eq}	0.2946 m
r_1	0.025 m
r_2	0.004 m
r_{joint}	0.0045 m
J_1	8.6×10^{-3} kg m^2
J_2	4.68×10^{-4} kg m^2
K_t	2.65 kg cm/A
K_n	Force/torque $=2\pi/0.005$
$K_{ax}K_tK_n$	2.3 N/V
$K_{ay}K_tK_n$	10.57 N/V
K_p	1.5

When the system's velocity response v reaches a steady state, i.e. $\dot{v}\cong 0$ and $v=v_{ss}$, Equation (3) equals the following:

$$T_d v_{ss}+T_f=K_pK_aK_tK_n(u-v_{ss}) \tag{4}$$

Namely, the input force $K_pK_aK_tK_n(u-v_{ss})$ to the IPCS is equal to the frictional force $T_d v_{ss}+T_f$. Varying the step command u from low velocity to high velocity yields the force set $K_pK_aK_tK_n(u-v_{ss})$ and the IPCS velocity response set v_{ss}. Meanwhile, the stiction force T_s is obtained by using the open-loop breakaway test. A voltage increase of 2^{-14} V/s is applied to the IPCS. T_s is obtained from the abrupt change in the IPCS position response with the threshold set at 2 encoder counts. Figure 5 plots the friction–velocity experimental data. The parameters of Tustin's friction model are obtained with the following procedures.

1. For the positive X-axis direction, when the speed is higher than the upper limit speed of the Stribeck friction region (about 0.0017 m/s), the friction–velocity relation forms a straight line:

$$f=T_c+T_d v \tag{5}$$

   Then, by the least-square method, one can obtain the viscous damping coefficient T_d and Coulomb friction force T_c.
2. When the speed is lower than the upper limit speed of the Stribeck friction region, rearranging (2) yields

$$\ln[(f-T_c-T_d v)/(T_s-T_c)]=-(v/v_s) \tag{6}$$

   The friction–velocity relation also becomes a straight line. Similarly, with known values on the left term of (6), one could obtain the slope $-(1/v_s)$ by the least-square method.

DOI: 10.1002/rnc

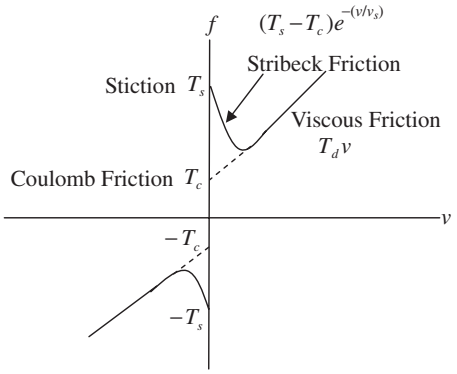

Figure 3. Tustin's friction model.

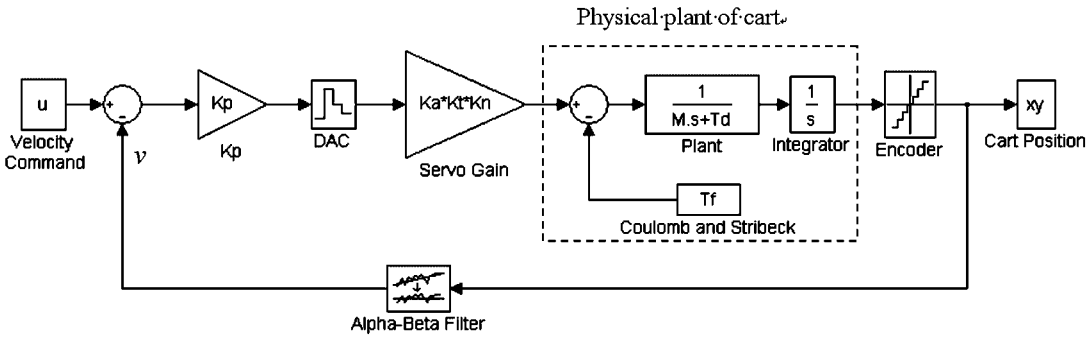

Figure 4. Control schema used in constructing Tustin's friction model.

Thus, Tustin's friction model for the positive X-axis direction is obtained. The model for the other direction or axis can also be obtained similarly. Finally, the equations for both axes are as follows:

$$f_x \begin{cases} f_{v_x^+} = [0.4151 + (0.54 - 0.4151)\mathrm{e}^{-(v_x^+/(7.389\times10^{-4}))} + 11.1871 v_x^+]\mathrm{N} \\ f_{v_x^-} = -[0.4701 + (0.55 - 0.4701)\mathrm{e}^{-(|v_x^-|/(8.392\times10^{-4}))} + 12.976|v_x^-|]\mathrm{N} \end{cases} \tag{7a}$$

$$f_y \begin{cases} f_{v_y^+} = [1.7789 + (2.4311 - 1.7789)\mathrm{e}^{-(v_y^+/(3.662\times10^{-3}))} + 54.7558 v_y^+]\mathrm{N} \\ f_{v_y^-} = -[2.116 + (2.9596 - 2.116)\mathrm{e}^{-(|v_y^-|/(4.094\times10^{-3}))} + 68.5919|v_y^-|]\mathrm{N} \end{cases} \tag{7b}$$

In relation to the pendulum joint friction, the Stribeck force cannot be experimentally observed, only viscous force and Coulomb force are considered. Considering the dynamics of pendulum (not inverted) including viscous friction and Coulomb friction with respect to the joint, one can obtain

DOI: 10.1002/rnc

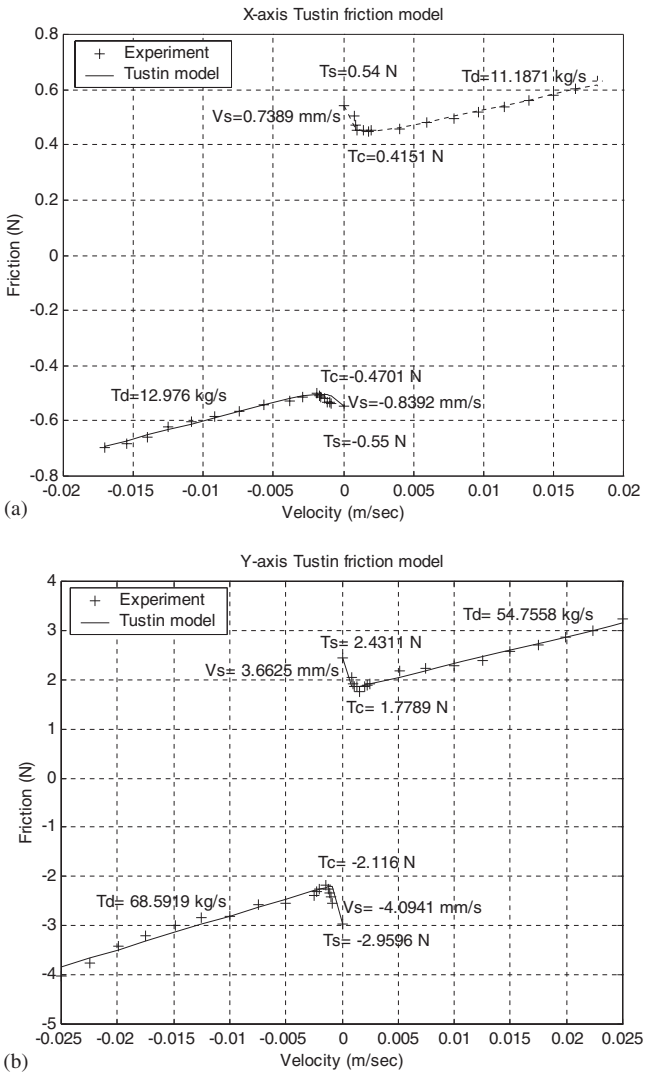

Figure 5. Friction–velocity map for the two axes: (a) X-axis and (b) Y-axis.

the following equation:

$$m_{\mathrm{eq}} l_{\mathrm{eq}}^2 \ddot{\Theta} + \mathbf{j}_{\mathrm{d}} r_{\mathrm{joint}}^2 \dot{\Theta} + m_{\mathrm{eq}} g l_{\mathrm{eq}} \sin\Theta - r_{\mathrm{joint}} \mathbf{j}_{\mathrm{c}} \mathrm{sgn}(\Theta) = 0 \tag{8}$$

where $\mathbf{j}_{\mathrm{d}} = [j_{\mathrm{d}_x} \;\; j_{\mathrm{d}_y}]^{\mathrm{T}}$, $\mathbf{j}_{\mathrm{c}} = [j_{\mathrm{c}_x} \;\; j_{\mathrm{c}_y}]^{\mathrm{T}}$.

Figure 6 illustrates the experimental and simulation results of the pendulum natural oscillation starting around 16° in θ/ϕ directions, respectively. The $\mathbf{j}_{\mathrm{c}}$ is obtained when the oscillations reach steady state, i.e. $\ddot{\Theta} = \dot{\Theta} = 0$ and $\Theta = 0.05°$ (1 count) and the $\mathbf{j}_{\mathrm{d}}$ is obtained from best fitting of the experimental data. They are listed as follows: $\mathbf{j}_{\mathrm{c}} = [0.168 \;\; 0.168]^{\mathrm{T}}$ N and $\mathbf{j}_{\mathrm{d}} = [45 \;\; 30]^{\mathrm{T}}$ kg/s.

DOI: 10.1002/rnc

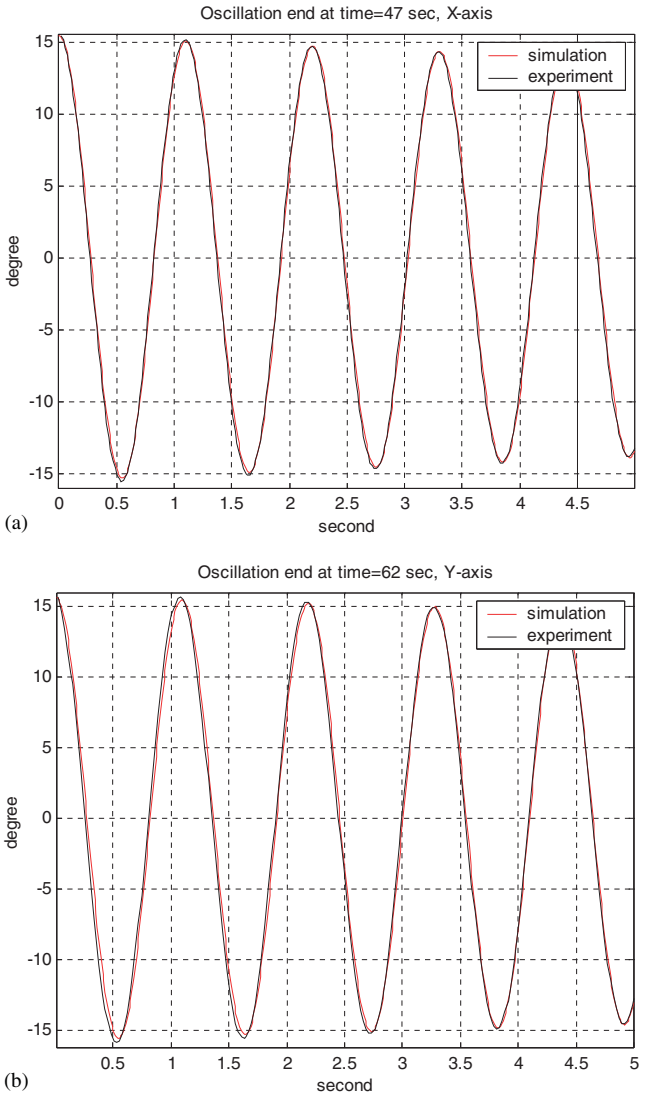

Figure 6. Natural oscillations of the pendulum in two directions: (a) X-axis and (b) Y-axis.

Since the frictional force of the physical plant depends on time, temperature, the position of the cart and other factors. The static Tustin's friction model cannot exactly model the frictional force at all times. Moreover, external disturbances and plant uncertainties will degrade the performance of the system. For the cart velocity feedback loop system, the DOB shown in Figure 7 is employed to solve this problem. In Figure 7, $\mathbf{P}(\mathbf{s}) = \mathbf{K}_a\mathbf{K}_t\mathbf{K}_n/(\mathbf{Ms}+\mathbf{T}_d)$ denotes the transfer function of cart model including the servo gain between cart velocity command and response; $\mathbf{P}_n(\mathbf{s})$ is nominal plant of $\mathbf{P}(\mathbf{s})$; d is disturbance; $\varsigma(\mathbf{s})$ is measurement noise. A DOB is generally introduced into motion control systems to eliminate the 'equivalent disturbance' as much as possible, and to

DOI: 10.1002/rnc

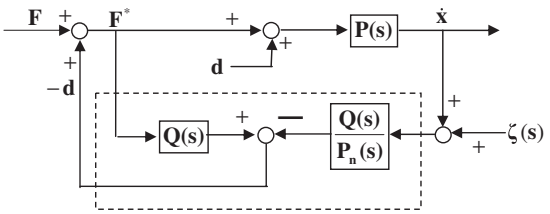

Figure 7. DOB structure (dashed line).

Table IV. Parameters of DOB.

$\mathbf{Q}(\mathbf{z})$	$\mathbf{P}_{\mathrm{n}}(\mathbf{s})$	$\frac{\mathbf{Q}}{\mathbf{P}_{\mathrm{n}}}(\mathbf{z})$
$\frac{0.4215z^{-1}+0.229z^{-2}}{1-0.5186z^{-1}+0.1691z^{-2}}$	$P_{\mathrm{n}x}(s)=\frac{2.3}{3.4s+12}$	$\frac{Q}{P_{\mathrm{n}x}}(z)=\frac{421.4768z^{-1}-418.083z^{-2}}{1-0.5186z^{-1}+0.1691z^{-2}}$
	$P_{\mathrm{n}y}(s)=\frac{10.57}{14.5s+61.68}$	$\frac{Q}{P_{\mathrm{n}y}}(z)=\frac{391.54z^{-1}-387.75z^{-2}}{1-0.5186z^{-1}+0.1691z^{-2}}$

force the actual system to become a nominal plant. The details of how a DOB works have been explained elsewhere [21]. In DOB, $\mathbf{Q}(\mathbf{s})$ can be interpreted as a complementary sensitivity function. Therefore, a sensible choice is to let the low-frequency dynamics of $\mathbf{Q}(\mathbf{s})$ closed to one for disturbance rejection and model uncertainties. In this study, a second-order Butterworth low-pass filter (LPF) [23]

$$\mathbf{Q}(\mathbf{s})=\frac{1}{(\mathbf{s}/\mathbf{w}_{\mathrm{c}})^2+\sqrt{2}(\mathbf{s}/\mathbf{w}_{\mathrm{c}})+1} \tag{9}$$

is designed so that the equation $\mathbf{Q}(\mathbf{s})/\mathbf{P}_{\mathrm{n}}(\mathbf{s})$ in DOB is a strict proper function. The cutoff frequency $\mathbf{w}_{\mathrm{c}}$ is designed at 100 Hz and the zero-order hold (ZOH) equivalence of analog filter is used to determine the digital Butterworth LPF $\mathbf{Q}(\mathbf{z})$. The parameters of DOB are listed in Table IV. Therefore, the DOB output $-\mathbf{d}(\mathbf{z})$ is obtained as

$$-\mathbf{d}(\mathbf{z})=\left[\mathbf{Q}(\mathbf{z})\mathbf{F}^{*}-\frac{\mathbf{Q}}{\mathbf{P}_{\mathrm{n}}}(\mathbf{z})\dot{\mathbf{x}}\right]\mathrm{N} \tag{10}$$

4. DESIGN OF CONTROL LAW

In this section, Tustin's friction model and the DOB are assumed to compensate for the friction and disturbance between the cart and the rail. The hybrid controller consisting of two controls is employed. One is a feedback linearization control for pendulum angle in the region of $3^\circ\leqslant|\Theta|\leqslant12^\circ$ and the other is an H_∞ control using LSDP in the region of $0^\circ\leqslant|\Theta|<3^\circ$.

4.1. The feedback linearization control for pendulum angle

Since the feedback linearization method is hardly used for both angle and position controls and in order to enhance the dynamic response of IPCS, the method is applied for pendulum angle in the

DOI: 10.1002/rnc

region of $3^\circ \leqslant |\Theta| \leqslant 12^\circ$. The control of the position of the cart is temporarily ignored and will be reactivated in $0^\circ \leqslant |\Theta| < 3^\circ$. A feedback linearization control is implemented to ensure the erection of the pendulum and to drive the angle of the pendulum into $0^\circ \leqslant |\Theta| < 3^\circ$. The control strategy provides the advantages of maximized operation angle of the pendulum and system robustness. The control law in this region is

$$\mathbf{F} = -\begin{bmatrix} -c_4c_6c_3c_0 & c_4c_6c_3c_1 \\ \bar{c}_4\bar{c}_6\bar{c}_3\bar{c}_1 & -\bar{c}_4\bar{c}_6\bar{c}_3\bar{c}_0 \end{bmatrix}^{-1} \begin{bmatrix} -c_4c_6c_3c_2 + c_4c_5 - c_4\tau_\theta + (k_{\dot\theta}\dot\theta + k_\theta\theta) \\ -\bar{c}_4\bar{c}_6\bar{c}_3\bar{c}_2 + \bar{c}_4\bar{c}_5 - \bar{c}_4\tau_\phi + (k_{\dot\phi}\dot\phi + k_\phi\phi) \end{bmatrix} \tag{11}$$

Setting $\mathbf{k}_\Theta = [k_\theta \;\; k_\phi]^{\mathrm{T}}$ and $\mathbf{k}_{\dot\Theta} = [k_{\dot\theta} \;\; k_{\dot\phi}]^{\mathrm{T}}$ as positive definite and substituting (11) into (1b) yields

$$\ddot\Theta + \mathbf{k}_{\dot\Theta}\dot\Theta + \mathbf{k}_\Theta\Theta = \ddot\Theta + (\boldsymbol{\lambda}_1 + \boldsymbol{\lambda}_2)\dot\Theta + (\boldsymbol{\lambda}_1\boldsymbol{\lambda}_2)\Theta = \left(\frac{\mathrm{d}}{\mathrm{d}\mathbf{t}} + \boldsymbol{\lambda}_1\right)\left(\frac{\mathrm{d}}{\mathrm{d}\mathbf{t}} + \boldsymbol{\lambda}_2\right)\Theta \tag{12}$$

where $\boldsymbol{\lambda}_i > 0$.

Therefore, Equation (12) is asymptotically stable. In this study, $\mathbf{k}_\Theta = [254.5 \;\; 145.6]^{\mathrm{T}}$, $\mathbf{k}_{\dot\Theta} = [32.02 \;\; 24.3]^{\mathrm{T}}$ and $\boldsymbol{\lambda}_i = (-17.3 - 14.7)/X\text{-axis}; (-13.5 - 10.8)/Y\text{-axis}$.

4.2. The H_∞ control using LSDP

Since the H_∞ control is designed in $0^\circ \leqslant |\Theta| < 3^\circ$, the model of (1) is linearized and decoupled as two independent subsystems. The linear state equation for the X-axis is

$$\begin{bmatrix} \dot x \\ \ddot x \\ \dot\theta \\ \ddot\theta \end{bmatrix} = \begin{bmatrix} 0 & 1 & 0 & 0 \\ 0 & 0 & \dfrac{-k_1^2 g}{k_{0x}k_2 - k_1^2} & 0 \\ 0 & 0 & 0 & 1 \\ 0 & 0 & \dfrac{k_{0x}k_1 g}{k_{0x}k_2 - k_1^2} & 0 \end{bmatrix} \begin{bmatrix} x \\ \dot x \\ \theta \\ \dot\theta \end{bmatrix} + \begin{bmatrix} 0 \\ \dfrac{k_2}{k_{0x}k_2 - k_1^2} \\ 0 \\ \dfrac{-k_1}{k_{0x}k_2 - k_1^2} \end{bmatrix} (F_x - f_x) + \begin{bmatrix} 0 \\ \dfrac{k_1}{k_{0x}k_2 - k_1^2} \\ 0 \\ \dfrac{-k_{0x}}{k_{0x}k_2 - k_1^2} \end{bmatrix} \tau_\theta + e_x \tag{13}$$

where e_x denotes the linearization error (including dynamic coupling effect), which is considered as input disturbance to the system. The estimate of $\|e_x\|$ is about 0.0129 for the underlying system. Similarly, the linear state equation of the Y-axis can be obtained by changing the (x, θ) with the (y, ϕ). Table V lists the open-loop characteristics of the IPCS revealing that the system is an unstable and a non-minimum phase system.

Table V. Characteristics of the pendulum–cart system.

Open-loop poles	$(0 \;\; 0 \;\; \pm 5.07)/X$-axis
$(m_1 = 250\,\mathrm{g}, l_1 = 32\,\mathrm{cm})$	$(0 \;\; 0 \;\; \pm 4.94)/Y$-axis
Open-loop poles	$(0 \;\; 0 \;\; \pm 10.49)/X$-axis
$(m_1 = 50\,\mathrm{g}, l_1 = 8\,\mathrm{cm})$	$(0 \;\; 0 \;\; \pm 10.4)/Y$-axis
Open-loop zeros for two axes	$(\pm 4.9)/(m_1 = 250\,\mathrm{g}, l_1 = 32\,\mathrm{cm})$
	$(\pm 10.38)/(m_1 = 50\,\mathrm{g}, l_1 = 8\,\mathrm{cm})$

DOI: 10.1002/rnc

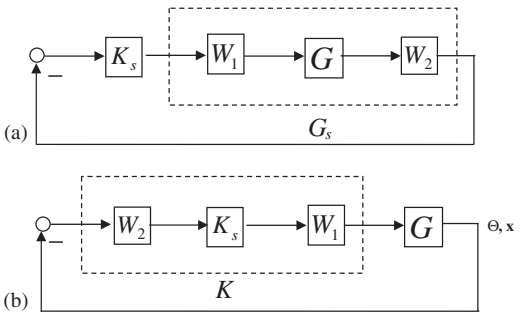

Figure 8. Loop shaping design procedure: (a) W_1, W_2 shaping the nominal plant G and (b) combining the K_s with the shaping functions W_1, W_2.

The LSDP includes three systematic procedures as follows [24].

1. *Loop shaping*: Figure 8(a) shows a pre-compensator W_1 and/or a post-compensator W_2 to shape the nominal plant G. The shaping functions W_1 and W_2 are combined to form the shaped plant $G_S = W_2 G W_1$, and G_S has a normalized left coprime factorization expression $G_S = M_s^{-1} N_s$. The singular values of the shaped plant G_S are high gain at low frequencies, low gain at high frequencies and the slope near the crossover frequencies should not be large.
2. Robustly stabilize the shaped plant G_S: A controller K_s internally stabilizes the nominal system G_S if and only if

$$\left\| \begin{bmatrix} K_s \\ I \end{bmatrix} (I - G_S K_s)^{-1} M_s^{-1} \right\|_\infty \leqslant \gamma \tag{14}$$

for a specific $\gamma > \gamma_{\min}$ ($\gamma = 1.1\gamma_{\min}$ in this study). The lowest achievable value of γ and the corresponding maximum stability margin ε were derived by McFarlane and Glover [25] as

$$\gamma_{\min} = \varepsilon_{\max}^{-1} = \{1 - \|[N_s \;\; M_s]\|_H^2\}^{-1/2} = (1 + \lambda_{\max}(XZ))^{1/2} \tag{15}$$

where $\lambda_{\max}$ denotes the spectral radius (maximum eigenvalue), and for a minimal state space realization (A,B,C,D) of G_S, Z and X are the unique positive-definite solutions to the following algebraic Riccati equations:

$$(A - BS^{-1}D^T C)Z + Z(A - BS^{-1}D^T C)^T - ZC^T R^{-1} CZ + BS^{-1}B^T = 0 \tag{16}$$

$$(A - BS^{-1}D^T C)^T X + X(A - BS^{-1}D^T C) - XBS^{-1}B^T X + C^T R^{-1} C = 0 \tag{17}$$

where $R = I + DD^T$, $S = I + D^T D$.

A controller K_s for a specific γ is obtained

$$K_s = \left[\begin{array}{c|c} A + BF + \gamma^2 (L^T)^{-1} ZC^T (C + DF) & \gamma^2 (L^T)^{-1} ZC^T \\ \hline B^T X & -D^T \end{array} \right] \tag{18}$$

where $F = -S^{-1}(D^T C + B^T X)$, $L = (1 - \gamma^2) I + XZ$.

3. The final feedback controller K for the plant G is then obtained by combining the K_s with the shaping functions W_1 and W_2 such that $K = W_1 K_s W_2$, Figure 8(b).

DOI: 10.1002/rnc

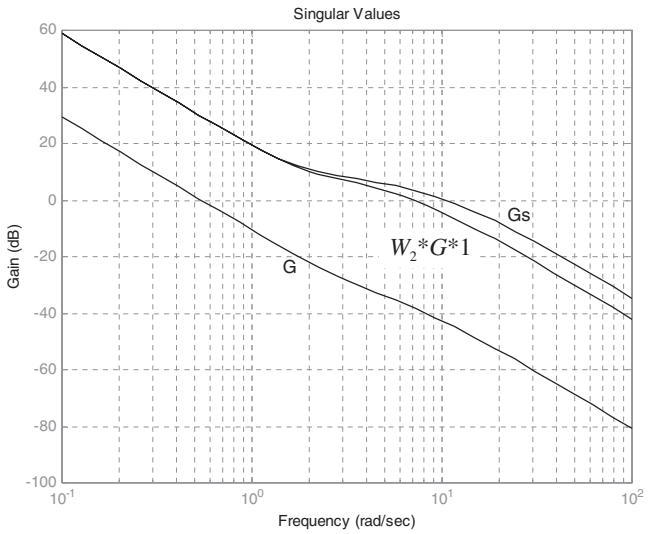

Figure 9. Open-loop singular values of nominal plant G, $W_2 * G * 1$ and shaped plant G_S.

The authors follow the above procedures to obtain the controller K and a stability margin $\varepsilon \leqslant \varepsilon_{\max}$. If $\varepsilon_{\max}$ is small, W_1 and W_2 should be adjusted so as the specific loop shape met the robust stability requirements and then K is re-evaluated.

In this study, considering the control energy and the angle of the pendulum is more important than the position of the cart, we select $W_1 = 2.4(s+5)/(s+12)$ and $W_2 = \left[\begin{smallmatrix} 30 & 0 \\ 0 & 90 \end{smallmatrix}\right]$. The open-loop singular values of G, $W_2 * G * 1$ and $G_S = W_2 G W_1$ are plotted in Figure 9. The value of γ is 4.01 (or stability margin $\varepsilon = 1/4.01$, which is much larger than the value of input disturbance $\|e_x\|$ in Equation (13)). The transfer functions of $\mathbf{F}_{\Theta_e}(\mathbf{s})/\mathbf{\Theta}_e(\mathbf{s})$ and $\mathbf{F}_{\mathbf{x}_e}(\mathbf{s})/\mathbf{x}_e(\mathbf{s})$ in the controller K are

$$\frac{\mathbf{F}_{\Theta_e}(\mathbf{s})}{\mathbf{\Theta}_e(\mathbf{s})} = \frac{-802.2s^5 - 21746s^4 - 216109s^3 - 1039525s^2 - 2556007s - 2720982}{s^5 + 55.38s^4 + 764.2s^3 + 3173.9s^2 + 2991s + 32.45} \tag{19a}$$

$$\frac{\mathbf{F}_{\mathbf{x}_e}(\mathbf{s})}{\mathbf{x}_e(\mathbf{s})} = \frac{-61.6s^5 - 2254.5s^4 - 33626.4s^3 - 208642s^2 - 492628s - 233563}{s^5 + 55.38s^4 + 764.2s^3 + 3173.9s^2 + 2991s + 32.45} \tag{19b}$$

The output of K is $\mathbf{F}(\mathbf{s}) = \mathbf{F}_{\Theta_e}(\mathbf{s}) + \mathbf{F}_{\mathbf{x}_e}(\mathbf{s})$. For implementing the controller, the fifth order (19) is reduced to the fourth order by using the balanced truncation method [26]. The controller K in the LSDP control for the two axes is the same. However, the amplifier gains (in the drivers) K_{ax}/K_{ay} are tuned in proportional to the cart mass m_{0x}/m_{0y} so that the two axes have similar transfer function.

5. EXPERIMENTAL RESULTS

For swing-up pendulum from rest (maximum inclination angle $\pm 18°$) into $|\Theta| \leqslant 12°$, one adopts a simple algorithm based on the following rationale. The torques due to gravity with respect to the

DOI: 10.1002/rnc

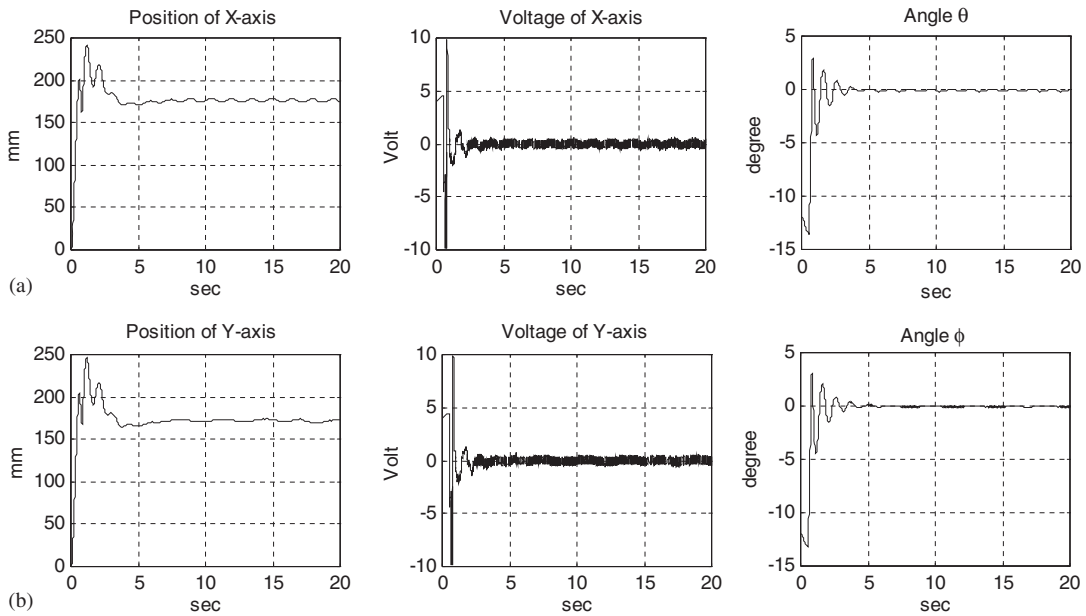

Figure 10. Bi-axial control performance of the hybrid controller: (a) position, control, and angle about the X-axis and (b) position, control, and angle about the Y-axis.

universal joint on the X–Z and Y–Z planes are obtained as follows:

$$-(m_1 l_1 + m_2 l_2) g \cos\phi \sin\theta \tag{20a}$$

$$-(m_1 l_1 + m_2 l_2) g \cos\theta \sin\phi \tag{20b}$$

The IPCS is accelerated by a force larger than Equations (20a) and (20b) for a short time and then pushed back immediately to generate a reverse torque to counteract (20a) and (20b). The swing-up algorithm is chosen as follows:

$$\mathbf{F} = \begin{cases} a\,\mathbf{sin}\Theta, & t \leqslant 0.5\,\mathrm{s} \\ -a\,\mathbf{sin}\Theta, & t > 0.5\,\mathrm{s} \end{cases}, \quad a = \frac{6}{\sin 18^\circ}\mathbf{K}_\mathrm{a}\mathbf{K}_\mathrm{t}\mathbf{K}_\mathrm{n} \tag{21}$$

Figure 10 plots the experimental data of the bi-axial hybrid control with friction compensation and DOB. Figures 11 and 12 illustrate the performances of the H_∞ control with/without friction compensation and DOB (Film: Friction_DOB). Table VI summarizes the control performances among several compensation strategies. The results show that the control strategy in this study is the best, which improves the control performance more than 7 times as compared with the method of no friction compensation. The following experiments are conducted to verify that the proposed control schema ensures the system stability and robustness.

1. Maximum operation angle (MOA) test: The MOA is an important performance index for the hybrid controller. The operation angle to trigger the controller is varied from $|\Theta| = 10^\circ$ to 18°. The rod is slowly pushed from rest to an angle Θ. When the pendulum rod reaches

DOI: 10.1002/rnc

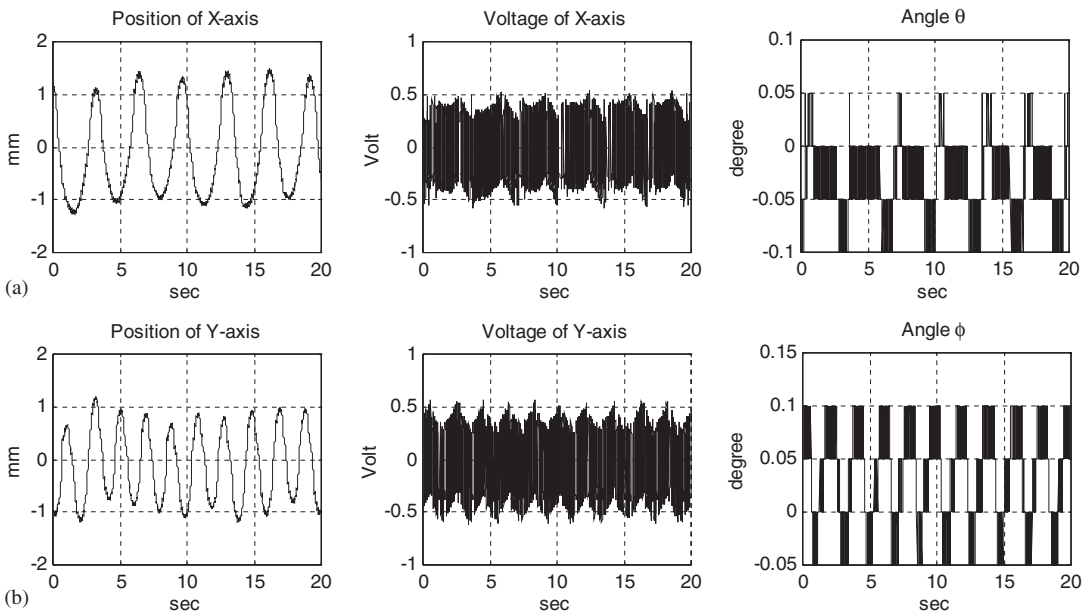

Figure 11. Performance of H_∞ control with friction compensation and DOB: (a) X-axis and (b) Y-axis.

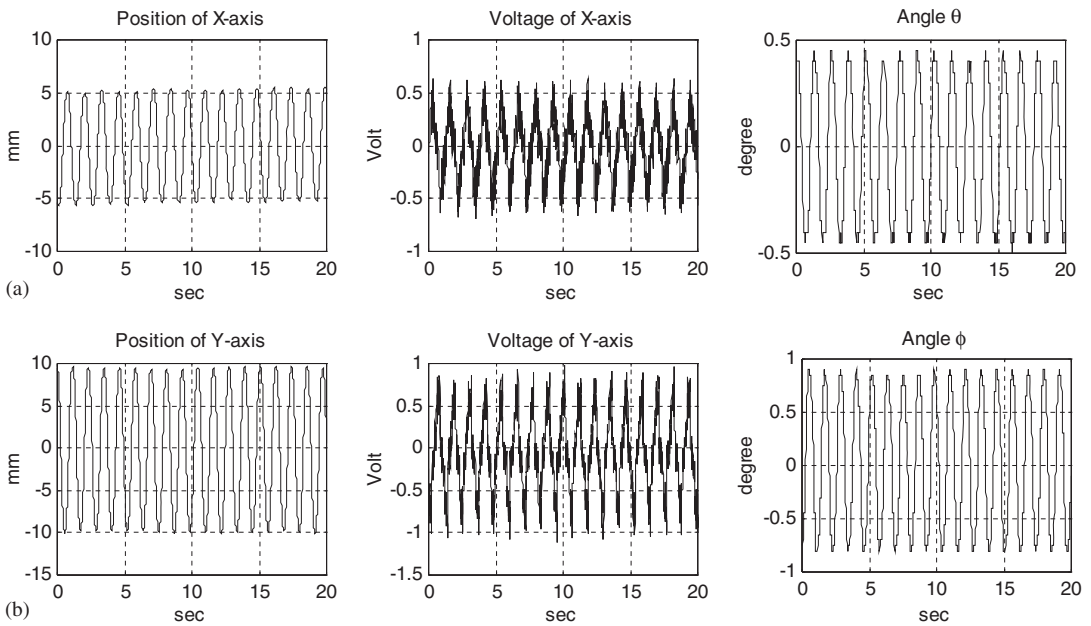

Figure 12. Performance of H_∞ control without friction compensation and DOB: (a) X-axis and (b) Y-axis.

DOI: 10.1002/rnc

Table VI. Comparison of steady-state error among several compensation strategies.

Control strategy	$\lvert\theta_e\rvert_{max}/\lvert\phi_e\rvert_{max}$	$\lvert x_e\rvert_{max}/\lvert y_e\rvert_{max}$
H_∞ + DOB + Tustin's model (this study)	0.1°/0.1°	1.4 mm/1.2 mm
H_∞	0.45°/0.85°	5.7 mm/10 mm
H_∞ + DOB	0.3°/0.75°	5.1 mm/8.5 mm
H_∞ + Tustin's model	0.1°/0.1°	1.6 mm/1.3 mm
H_∞ + (Tustin's—Coulomb)	0.3°/0.75°	4.5 mm/9 mm
H_∞ + (Tustin's—viscous)	0.1°/0.1°	2.1 mm/1.6 mm
H_∞ + (Tustin's—Stribeck)	0.1°/0.1°	1.8 mm/1.5 mm

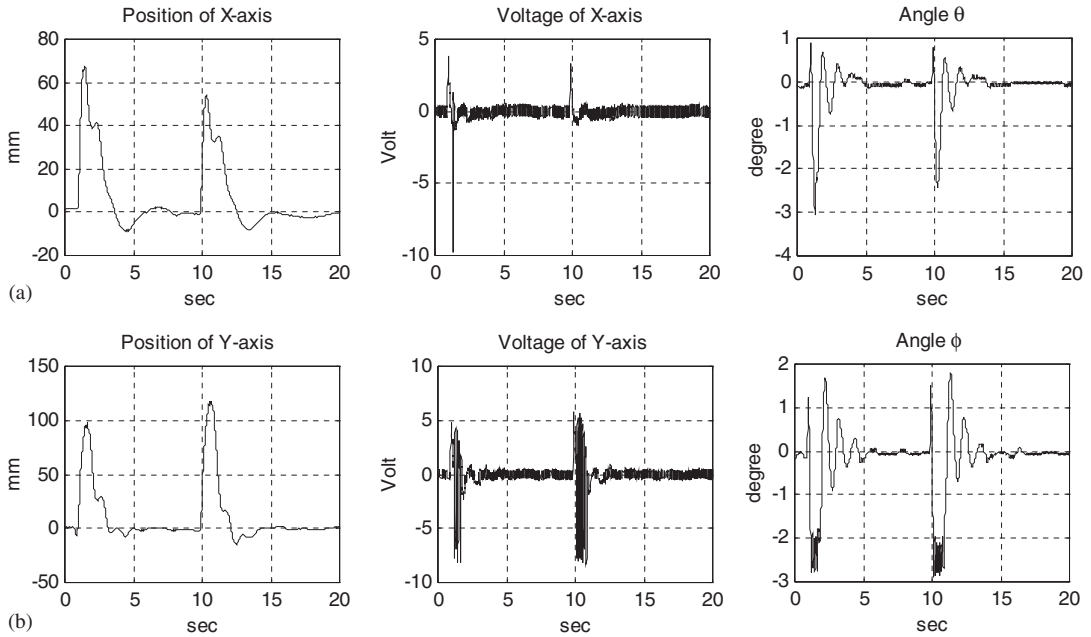

Figure 13. A 9 V battery impacts on the head of the pendulum at 1 and 9.9 s: (a) X-axis and (b) Y-axis.

angle Θ, a small force is applied to the rod to push it into the hybrid controller and to determine whether the pendulum is erect. This procedure is repeated on the X-axis/Y-axis. The MOA is obtained $|\Theta|_{max} = [14^\circ \ 12^\circ]^T$ (Film: MOA_Test). Moreover, if only the H_∞ control is active, the MOA is $|\Theta|_{max} = [8^\circ \ 7^\circ]^T$.

2. A 9 V battery is used to impact the pendulum head to verify the system robustness. Figure 13 is the experimental data and the impacts applied at 1 and 9.9 s, respectively. For showing the system's non-minimum phase phenomenon, a 75 mm rapid shift backward and forward of the IPCS is performed. Figure 14 is the experimental data and the non-minimum phase phenomenon of the cart position occurs at 0.4 and 10.4 s in the sub-figures 'Position of X-axis/Y-axis' (Film: Swing_Impact_75mmShift).

DOI: 10.1002/rnc

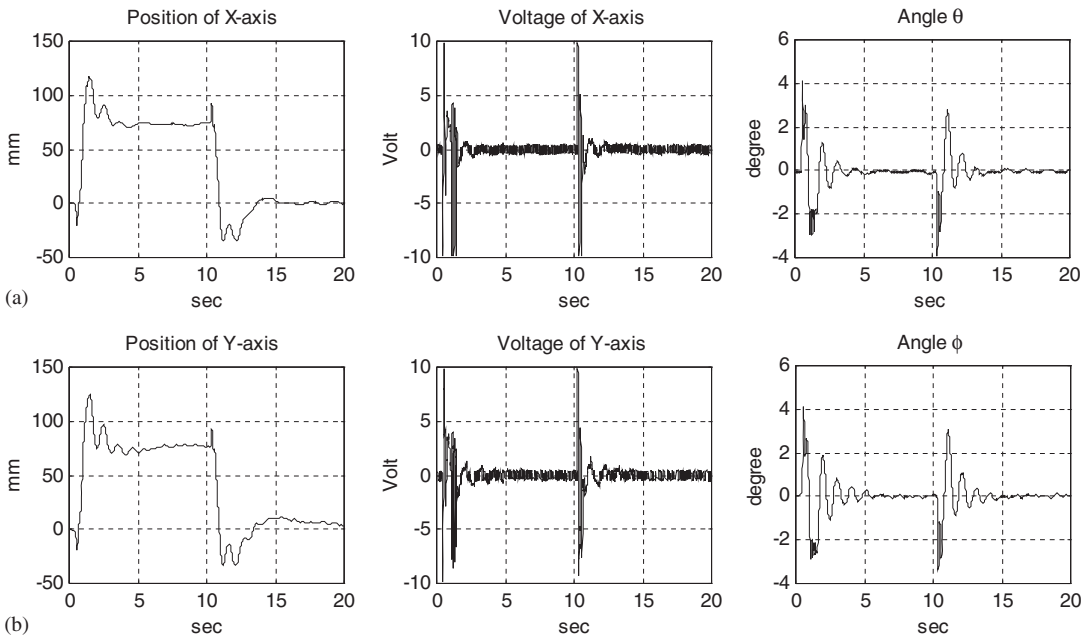

Figure 14. The non-minimum phase phenomenon occurs at 0.4 and 10.4 s: (a) X-axis and (b) Y-axis.

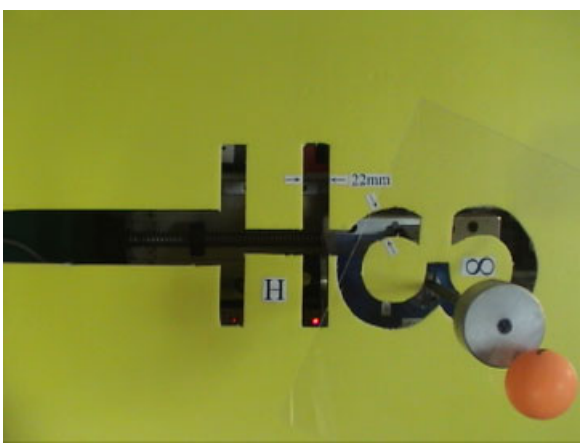

Figure 15. The pendulum–cart with a ping-pong ball shifted inside the H_∞-form slot.

3. An H_∞-form slot shown in Figure 15 is used to show the tracking control of the bi-axial IPCS. In this experiment, the X-axis is inclined at 10° and the Y-axis remains horizontal (shown in film). A square transparent acrylic plate with a width of 200 mm is mounted on the top of the pendulum and a ping-pong ball falls free at a height of 50 mm above the plate. Then, the H_∞-form plastic plate with a slot width of 22 mm is inserted into the pendulum

DOI: 10.1002/rnc

rod and the IPCS with a moving step size of 0.1 mm is shifted within the slot to demonstrate the system stability (Film: H-infinity_Slot).

4. A 9 V battery impacts on a 50 g pendulum head at a height of 8 cm above the universal joint to verify the system robustness with parameters variation (see Figure 1). The typical values of the system in the previous experiments are 250 g pendulum head at a height of 32 cm (Film: 50gHead_8cmHeight).

6. DISCUSSION

1. In Table VI, it is observed that Tustin's friction compensation is more critical than the DOB compensation. As for Tustin's friction model, compensation for the Coulomb force is more important than that for the viscous force; notably, Stribeck force compensation also contributes to the performance of the system.
2. In Figure 11, since it is difficult to obtain the vertical reference point of pendulum angle in experiments, the data of 'angle θ/ϕ' has one count (0.05°) bias error.

7. CONCLUSION

In this study, the hybrid control with Tustin's friction model and the DOB compensation have been successfully applied to a bi-axial IPCS. The experimental results show that the proposed control schema that improves the SSE more than 7 times and enlarge the MOA more than 1.7 times can effectively control the IPCS. Moreover, experimental films are provided at the web site http://hinfinity.myweb.hinet.net to show the effectiveness and robustness of the control schema.

REFERENCES

1. Furuta K, Kajiwara H, Kosuge K. Digital control of a double inverted pendulum on an inclined rail. *International Journal of Control* 1980; **32**(5):907–924.
2. Tsachouridis VA, Medrano-Cerda GA. Discrete-time H_∞ control of a triple inverted pendulum with single control input. *IEE Proceedings—Control Theory and Applications* 1999; **146**(6):567–577.
3. Chen YP, Chang JL, Chu SR. PC-based sliding-mode control applied to parallel-type double inverted pendulum system. *Mechatronics* 1999; **9**(5):553–564.
4. Lin CE, Sheu YR. A hybrid-control approach for pendulum-car control. *IEEE Transactions on Industrial Electronics* 1992; **39**(3):208–214.
5. Chen CS, Chen WL. Robust adaptive sliding-mode control using fuzzy modeling for an inverted-pendulum system. *IEEE Transactions on Industrial Electronics* 1998; **45**(2):297–306.
6. Lozano R, Fantoni I, Block DJ. Stabilization of the inverted pendulum around its homoclinic orbit. *Systems and Control Letters* 2000; **40**:197–204.
7. Huang SJ, Huang CL. Control of an inverted pendulum using grey prediction model. *IEEE Transactions on Industry Applications* 2000; **36**(2):452–458.
8. Rubí J, Rubio Á, Avello A. Swing-up control problem for a self-erecting double inverted pendulum. *IEE Proceedings—Control Theory and Applications* 2002; **149**(2):169–175.
9. Sprenger B, Kucera L, Mourad S. Balancing of an inverted pendulum with a SCARA robot. *IEEE/ASME Transactions on Mechatronics* 1998; **3**(2):91–97.
10. Cho HT, Jung S. Balancing and position tracking control of an inverted pendulum on an X–Y plane using decentralized neural networks. *Proceedings of the 2003 IEEE/ASME International Conference on Advanced Intelligent Mechatronics* (*AIM 2003*), Kobe, Japan, 2003; 181–186.

DOI: 10.1002/rnc

11. Wai RJ, Chang LJ. Adaptive stabilizing and tracking control for a nonlinear inverted-pendulum system via sliding-mode technique. *IEEE Transactions on Industrial Electronics* 2006; **53**(2):674–692.
12. van der Linden GW, Lambrechts PF. H_∞ control of an experimental inverted pendulum with dry friction. *IEEE Control Systems Magazine* 1993; **13**(4):44–50.
13. Grasser F, D'Arrigo A, Colombi S, Rufer AC. JOE: a mobile, inverted pendulum. *IEEE Transactions on Industrial Electronics* 2002; **49**(1):107–114.
14. Olfati-Saber R. Nonlinear control of underactuated mechanical systems with applications to robotic and aerospace vehicles. *PhD Thesis*, Department of Electrical Engineering and Computer Science, Massachusetts Institute of Technology, Cambridge, MA, 2001.
15. Aguilar-Ibañez C, Gutierrez FO. A simple model matching for the stabilization of an inverted pendulum–cart system. *International Journal of Robust and Nonlinear Control* 2007; **18**(6):688–699.
16. Aguilar-Ibañez C, Gutiérrez FO, Suarez-Castañon S. Lyapunov-based controller for the inverted pendulum–cart system. *Nonlinear Dynamics* 2005; **40**(4):367–374.
17. Aguilar-Ibañez C, Gutierrez FO, Sossa AH. Lyapunov approach for the stabilization of the inverted spherical pendulum. *Proceedings of the 45th IEEE Conference on Decision and Control*, San Diego, CA, U.S.A., 2006; 6133–6137.
18. Tustin A. The effects of backlash and of speed-dependent friction on the stability of closed-cycle control systems. *Journal of the Institution of Electrical Engineers* 1947; **94**(2A):143–151.
19. Armstrong-Hélouvry B, Dupont P, Canudas de Wit C. A survey of models, analysis tools and compensation methods for the control of machines with friction. *Automatica* 1994; **30**(7):1083–1138.
20. Canudas de Wit C, Olsson H, Astrom KJ, Lischinsky P. A new model for control of systems with friction. *IEEE Transactions on Automatic Control* 1995; **40**(3):419–425.
21. Lee HS, Tomizuka M. Robust motion controller design for high-accuracy positioning systems. *IEEE Transactions on Industrial Electronics* 1996; **43**(1):48–55.
22. Edward PC. *Digital Filtering*: *An Introduction*. Houghton Mifflin: Boston, 1992.
23. Millman J. *Microelectronics*: *Digital and Analog Circuits and Systems*. McGraw-Hill: New York, 1979.
24. Skogestad S, Postlethwaite I. *Multivariable Feedback Control*: *Analysis and Design*. Wiley: New York, 1996.
25. McFarlane DC, Glover K. *Robust Controller Design Using Normalized Coprime Factor Plant Descriptions*. Lecture Notes in Control and Information Sciences, vol. 138. Springer: Berlin, 1990.
26. Zhou K. *Essentials of Robust Control*. Prentice-Hall: Englewood Cliffs, NJ, 1998.

DOI: 10.1002/rnc